Article

Screening metal-organic frameworks for adsorption-driven osmotic heat engines via grand canonical Monte Carlo simulations and machine learning

High-throughput computational screening

Machine learning

Rui Long, Xiaoxiao Xia, Yanan Zhao, Song Li, Zhichun Liu, Wei Liu

songli@hust.edu.cn (S.L.)
zcliu@hust.edu.cn (Z.L.)

HIGHLIGHTS

Structure-property relationship of MOFs are revealed via GCMC

Qualified absorbents are of larger LCD and ASA and moderate adsorption enthalpy

Optimal MOF structure properties are obtained through machine learning

Article

Screening metal-organic frameworks for adsorption-driven osmotic heat engines via grand canonical Monte Carlo simulations and machine learning

Rui Long,[1] Xiaoxiao Xia,[1] Yanan Zhao,[1] Song Li,[1,*] Zhichun Liu,[1,2,*] and Wei Liu[1]

Summary

Adsorption-driven osmotic heat engines offer an alternative way for harvesting low-grade waste heat below 80°C. In this study, we performed a high-throughput computational screening based on grand canonical Monte Carlo simulations to identify the high-performance metal-organic frameworks (MOFs) from 1322 computationally ready experimental MOF structures for adsorption-driven osmotic heat engines with LiCl-methanol as the working fluid. Structure-property relationship analysis reveals that MOFs exhibiting high energy efficiency possess large working capacity, pore size and surface area, and moderate adsorption enthalpy comparable to the evaporation enthalpy. Furthermore, machine learning is employed to accelerate the computational screening for satisfied MOFs via the structure properties. The optimal structure properties of the MOFs are further identified via the ensemble-based regression model by optimizing the energy efficiency via the genetic algorithm, which shed light on rationally designing and fabricating MOFs for desired heat-to-electricity conversion.

Introduction

Most of global industrial and civil energy supply originates from the fossil resources. The nature and environment have suffered much from the over exploitation and massive combustion of fossil fuels (Chu and Majumdar, 2012). Over 70% of the primary energy is discharged to the atmosphere in the form of waste heat (Forman et al., 2016), of which over 60% belongs to low-grade waste heat with the temperature below 100°C (Forman et al., 2016). To efficiently harvest such low-grade waste heat, efforts have been devoted to developing suitable heat-to-power conversion technologies such as semiconductor-based thermoelectric devices and alternative thermodynamic cycles (Bell, 2008; Tritt and Subramanian, 2006; Chen et al., 2003; Long et al., 2020; Lee et al., 2014).

Recently, osmotic heat engines (OHEs) consisting of a solution regeneration module and power generation module have attracted increasing attentions due to their higher theoretic efficiency than conventional heat-to-electricity technologies for harvesting low-grade waste heat (Zhao et al., 2020a; Hu et al., 2019). In the solution regeneration module, salt solution is driven by the low-grade heat source and separated into concentrated and diluted streams via distillation technologies such as membrane distillation (MD) and multieffect distillation (MED) (Long et al., 2018; Li et al., 2020b). The Gibbs free energy of mixing of the regenerated solutions at different concentrations is then converted to electric power via reverse electrodialysis (RED) or pressure-retarded osmosis (PRO) power generation system (Ortega-Delgado et al., 2019; Post et al., 2007). The RED process is driven by the transmembrane salinity gradient, in which cations and anions diffuse through cation exchange membranes and anion exchange membranes, thus to build up the ionic current and extract electricity by an external load (Chanda and Tsai, 2019; Tian et al., 2020; Long et al., 2019). In the PRO process, the low concentration solvent permeates into the pressurized high concentration side under osmotic pressure difference, then is depressurized via a hydro-turbine for power generation (Benjamin et al., 2020).

Tamburini et al. (Tamburini et al., 2017) investigated an OHE which couples MED with RED to convert low-grade heat into electric power, and a power density of about 18W/m^2 was obtained at 5 M NaCl solution when working between 90°C and 25°C. Lee et al. (Lee et al., 2015) employed a multi-stage vacuum

[1]School of Energy and Power Engineering, Huazhong University of Science and Technology, Wuhan 430074, P. R. China

[2]Lead contact

*Correspondence:
songli@hust.edu.cn (S.L.),
zcliu@hust.edu.cn (Z.L.)

MD integrated with PRO to harvest waste heat, achieving a maximum power density of 9.7W/m^2. Long et al. (Long et al., 2017) presented an alternative hybrid membrane-driven OHE composed of MD and RED; an electrical efficiency of 1.15% was achieved with the heat source temperature of 60°C and 5 mol/kg NaCl solution as working fluid. Adsorption-driven desalination (AD) as thermally driven technology is promising for solution regeneration due to the relative low energy consumption and low operating temperature (Chua et al., 1999; Dakkama et al., 2017; Olkis et al., 2019; Thu et al., 2017). Olkis et al. (Olkis et al., 2018) proposed an AD-RED to extract electricity from waste heat with an exergy efficiency of 30%, indicating the potential application of the AD-RED hybrid system. Zhao et al. (Zhao et al., 2020a, 2020b) presented an adsorption-driven cogeneration system for simultaneously providing cooling power and generating electricity by utilizing low-grade heat with a maximum exergy efficiency of 33.9%.

The performance of adsorption-driven solution regeneration process is mainly determined by the adsorption characteristics of the adsorbents, thus selecting high-performing adsorbents is critical to improve the energy efficiency of adsorption-driven OHEs. There are various adsorbents that can be employed for adsorption, such as silica gel, activated carbons, zeolites, and metal-organic frameworks (MOFs) (Wu et al., 2016; Erdős et al., 2018; Li et al., 2020a). Among these adsorbents, MOFs attracted considerable attentions because of their outstanding adsorption performance due to the high volumetric surface area, structural diversity, and structural tunability (Li et al., 2016, 2019b; Altintas et al., 2018; Kirchon et al., 2018). Screening potential MOFs from a vast number of MOF databases for adsorption-driven heat pumps and chillers has been extensively investigated in recent decades (Liu et al., 2020; Shi et al., 2020). A high-throughput computational screening of MOFs for alcohol-based adsorption-driven heat pumps based on grand canonical Monte Carlo has been conducted in our previous study (Li et al., 2019a), from which the correlation between MOF structure property and their coefficient of performance (COP), as well as the top performers with the highest COP, were identified. A computational screening of 2930 MOFs for adsorption-driven heat pumps and chillers has also reported, and six structures with the highest working capacities were obtained (Erdős et al., 2018). Shi et al. (Shi et al., 2020) conducted a high-throughput computational screening of 6013 computation-ready experimental MOFs to select the suitable methanol-MOF working pair for adsorption-driven heat pumps, and 30 MOFs were selected as promising candidates.

To achieve appealing energy conversion efficiency of adsorption-driven OHEs, high-throughput computational screening of high-performing MOF adsorbents is highly demanded. Therefore, in this work, high-throughput computational screening of MOF adsorbents for the adsorption-driven heat engines with LiCl-methanol solutions as the working fluids has been carried out. Methanol was used as solvents owing to its high evaporation pressure that is favorable for the effective mass transfer within adsorbents. The methanol adsorption performance of 1322 computationally ready experimental (CoRE) MOFs was evaluated by the grand canonical Monte Carlo (GCMC) simulation, from which the energy conversion efficiency to electricity of each MOF was derived for the first time. Moreover, the relationship between MOF structure property and energy efficiency of adsorption-driven heat engines is systematically analyzed to facilitate the rational design of high-performance MOFs in future. In order to further accelerate the computational screening of MOF adsorbents, machine learning by various classification and regression models optimized by the Bayesian optimization has been conducted, demonstrating a more efficient approach to identify top performers from a given database without exhaustive computation. The correlation between MOF structure property and energy efficiency is validated, and the optimal structure properties are identified via the ensemble-based regression model by optimizing the energy efficiency based on the genetic algorithm (GA). The structure-property relationship extracted in this work may provide insightful guidance for quick exploration of high-performance MOFs and facilitates rational design of efficient MOFs for upgraded heat-to-electricity conversion of adsorption-driven OHEs.

Results and discussion

Adsorption-driven osmotic heat engines

As shown in Figure 1, the adsorption-driven OHE consists of an adsorption-driven solution regeneration process and a power generation process. In the solution regeneration process, the salt-methanol solution is separated into concentrated and diluted solutions via the adsorption-driven separation cycle driven by the external low-grade heat. In the power generation process, a PRO is employed to covert the Gibbs free energy of mixing of the regenerated solutions at different concentrations via a hydro-turbine.
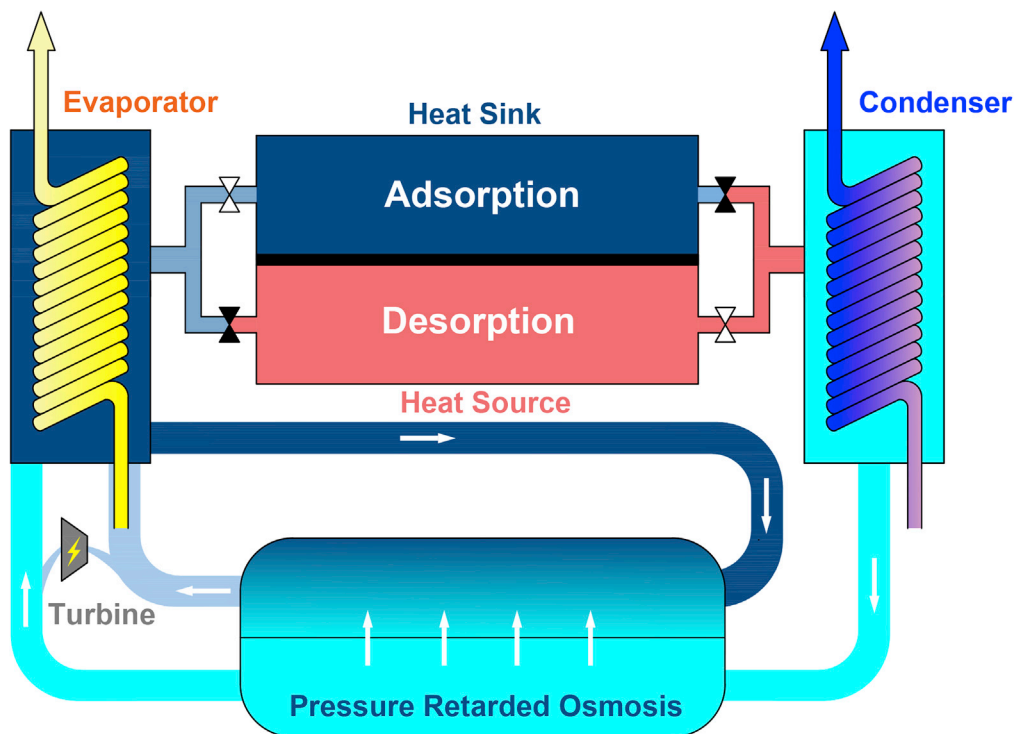
Figure 1. Schematic diagram of the adsorption-based osmotic heat engine

The isosteric diagram of the adsorption-driven separation cycle is shown in Figure 2. The adsorption-driven separation cycle originates from the alternatively operated adsorption process and desorption processes. The working salt-methanol solution is evaporated in the evaporator at the environment temperature. The methanol vapor is then adsorbed by the adsorbent meanwhile releasing the sorption heat. The adsorbent is cooled by the external cooling circuit. The adsorbent is then heated for desorption with pressure increased to the condensing pressure. In the desorption process, driven by the external heat source, methanol is desorbed from the adsorbent and then enters into the condenser for condensing. Thereafter, the adsorbent is further cooled for adsorption. The condensing temperature is also maintained at the environment via external cooling circuit. Although the evaporating and condensing temperatures are identical, the pressure of evaporating and condensing processes is different. The dissolved salt in the salt-methanol solution lowers its saturation pressure, which could be calculated via the solution activity:

$$p_{sat,ss} = a_s p_{sat,ps}, \quad \text{where} \quad a_s = \exp(-vCM\Phi) \qquad \text{(Equation 1)}$$

where v is the number of dissociated ions and C is the molarity, M is the mole mass, and Φ is the osmotic coefficient. The subscripts ss and ps denote salt solution and pure solution, respectively.

Total heat in the methanol regeneration process (isosteric heating and isobaric desorption) is calculated according to the following equation (Supplemental Information):

$$Q_{reg} \approx m_{sb} c_p^{sb} \Delta T - \frac{1}{M} \rho_{liq} \langle \Delta_{ads}H \rangle \Delta W m_{sb} \qquad \text{(Equation 2)}$$

where ΔW is the working capacity of the AD system, and W is the adsorption uptake that is determined by process temperature and pressure. c_p^{sb} is the specific heat capacity of the adsorbent. m_{sb} is the mass of the adsorbent. ρ_{liq} is the density of the liquid methanol. $\Delta T = T_3 - T_1$ is the temperature difference in the heating process. $\langle \Delta_{ads}H \rangle$ is the average adsorption enthalpy, which is calculated as follows:

$$\langle \Delta_{ads}H \rangle = \frac{\Delta_{ads}H_{max} + \Delta_{ads}H_{min}}{2} \qquad \text{(Equation 3)}$$

where $\Delta_{ads}H_{max}$ and $\Delta_{ads}H_{min}$ are the adsorption enthalpy at the maximum and minimum adsorption uptakes in the adsorption process.
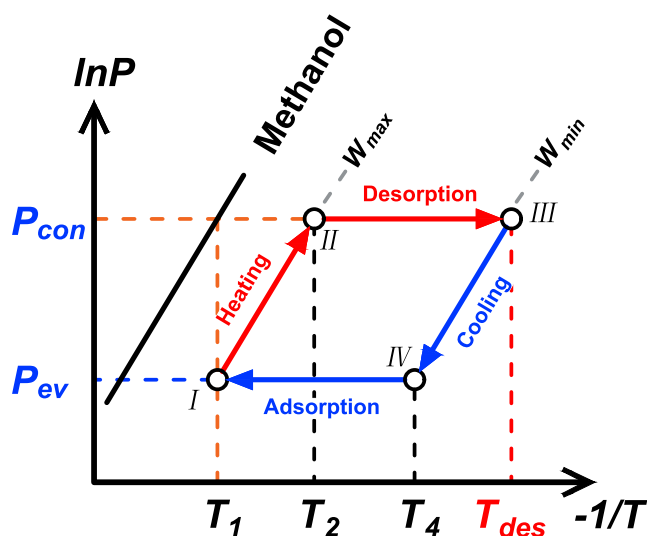
Figure 2. Isosteric diagram of the adsorption-driven separation cycle
The temperatures during the evaporating and condensing processes are equal ($T_{eva} = T_{con}$). The evaporating pressure (P_{eva}) is lower than the condensing pressure (P_{con}) due to dissolved salts.

Concentrated and diluted salt-methanol solutions generated in the adsorption-driven separation cycle enter into the PRO module for power generation. In the PRO process, driven by the osmotic pressure difference between the draw and permeate solutions, the solvent permeates through a semipermeable membrane from the low concentration side to the pressurized high concentration side. The transmembrane solvent is then depressurized through a turbine for power generation. The work of the downstream PRO system achieves its maximum value of $W_{PRO} = \nu R \Phi T_1 C_1 \Delta W m_{sb}$ when the produced pure methanol in the adsorption-driven solution regeneration system equals to the transmembrane methanol in the PRO system. In this case, the applied pressure equals to the osmotic pressure at the working concentration C_1 (initial salt concentration in the evaporator). Relevant analysis can be found in the Supplemental Information.

The energy efficiency of the adsorption-driven OHE is calculated as follows:

$$\eta = \frac{W}{Q_{reg}} = \frac{\nu R \Phi T_1 C_1 \Delta W}{c_p^{sorbent} \Delta T - \frac{1}{M_w} \rho_{liq} \langle \Delta_{ads} H \rangle \Delta W} \qquad \text{(Equation 4)}$$

Generally, the working solutions in the adsorption-driven OHEs can be prepared by dissolving organic or inorganic salts into the solvents such as water, methanol, and ethanol. Compared to water solutions, methanol solutions are employed here due to its high vapor pressure that is favorable for the mass transfer (de Lange et al., 2015a). Due to relatively large solubility and osmotic coefficient, here LiCl-methanol solution is employed as the working fluid of the OHEs. According to Equation (4), the energy efficiency of OHEs using different MOF adsorbents can be evaluated under the given working fluid and operation conditions. Here, the evaporation and condensation temperatures are both 20°C. The molality of the LiCl-methanol working concentration is 6 mol/kg. The saturation pressure of methanol at 20°C is 13,030 Pa. The saturation pressure of 6 mol/kg LiCl-methanol solution at 20°C is 4480 Pa. Our GCMC simulations were performed at T_{ads} = 293.15 K, P_{eva} = 4480 Pa, and T_{des} = 353.15 K, P_{con} = 13030Pa to determine the corresponding working capacity and adsorption enthalpy, thus to calculate the energy efficiency.

Relationships between structure property, adsorption performance, and the energy efficiency

The solution separation degree of the LiCl-methanol solution in the adsorption-driven regeneration process plays a dominant role on the overall heat-to-electricity conversion efficiency. High working capacity (ΔW) suggests that the working salt solution can be better separated, indicating more work can be extracted in the following the power generation process. The working capacity is significantly correlated with the structure property and adsorption characteristics of the MOFs including largest cavity diameter
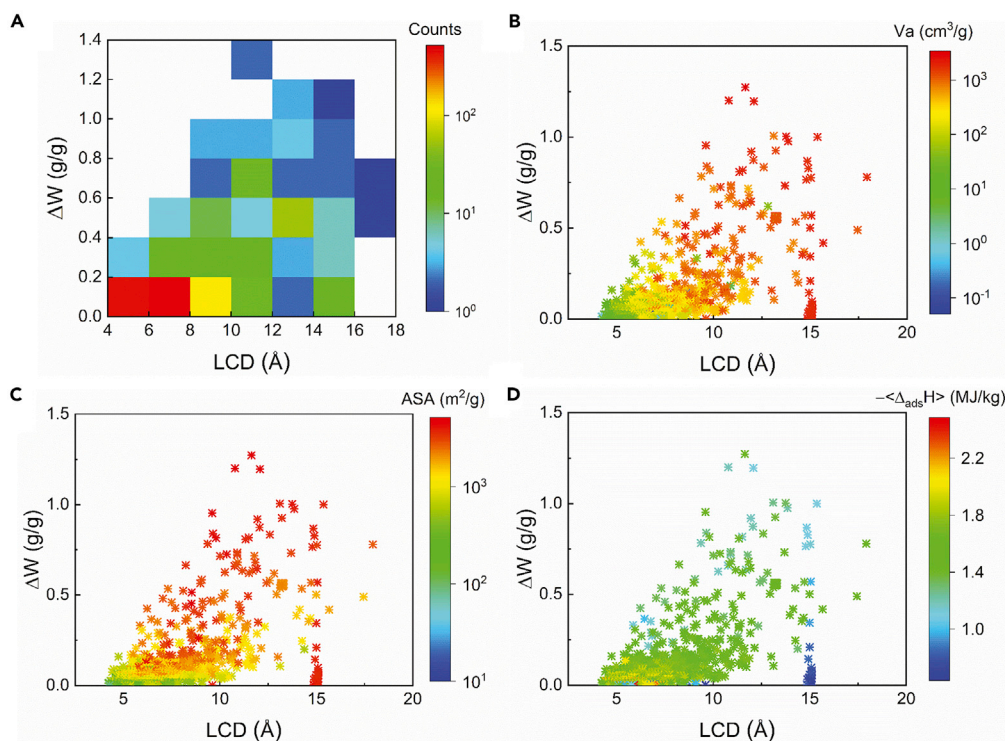
Figure 3. Predicted *ΔW* values of 1322 CoRE MOFs as a function of LCD

The data were colored by (A) MOF numbers, (B) V_a, (C) ASA, and (D) $-\langle\Delta_{ads}H\rangle$. The number of the MOFs in each square of (A) was calculated with an interval of LCD = 2 Å and *ΔW* = 0.2 g/g.

(LCD), available pore volume (V_a), accessible surface area (ASA), and heat of adsorption ($\langle\Delta_{ads}H\rangle$). Such correlations were obtained by analyzing the results from the first-round screening of 1322 CoRE MOFs based on GCMC simulations. The relation between the LCD and the working capacity is depicted in Figure 3. The capillary condensation may occur when the pore diameter is larger than the critical diameter $D_c = 4\sigma T_c/(T_c - T)$ at the condensing temperature T (Coasne et al., 2013; Canivet et al., 2014), where σ is the approximate size of a methanol molecule (i.e. 0.36 nm). T_c is the critical temperature, which 512.6 K for methanol in this work. In present working conditions, $D_c = 33.6$ Å at 293.15 K. All the maximum pore sizes of the investigated MOFs are smaller than the critical diameter for methanol condensation, indicating the reversible adsorption behavior and unlikely capillary condensation under given working conditions. Most MOFs exhibited the pore sizes between 4 Å −10 Å with the lower working capacity than 0.2 g/g. *ΔW* increases with increasing LCD until 12 Å where the maximum value of approximately 1.4 g/g is achieved. When LCD is greater than 14 Å, the working capacity decreases. MOFs with a relatively high working capacity (*ΔW* > 0.8 g/g) exhibited pore sizes between 8 Å −16 Å, V_a > 1000 cm³/g, ASA>3300 m²/g, and $\langle\Delta_{ads}H\rangle$ of about −1.25MJ/kg that is close to the evaporation enthalpy of methanol ($\langle\Delta_{ads}H\rangle$=1.18MJ/kg). $\langle\Delta_{ads}H\rangle$ generally decreases with the increasing pore size, similar to the previous finding for MOF-methanol, MOF-ethanol, and MOF-water working pairs for adsorption heat transformers (de Lange et al., 2015a, 2015b).

The correlations between the MOF structure property and the energy efficiency of adsorption-driven OHE are depicted in Figure 4. Most MOFs with the pore sizes between 4 Å-10 Å exhibited the energy efficiency less than 5%. The energy efficiency generally increases with LCD until 16 Å. Such a trend can be ascribed to the increased methanol working capacity (*ΔW*) of MOFs with the LCD as presented in Figure 3C, which directly contributes to the improved energy efficiency according to Equation 4. MOFs with large pore sizes or pore volumes are a prerequisite for the desired stepwise adsorption isotherm that is favorable for solution separation and the energy efficiency (de Lange et al., 2015b). The stepwise adsorption in large pore-sized MOFs under the given operating conditions along with the high working capacity and suitable heat of adsorption is beneficial for high energy efficiency.
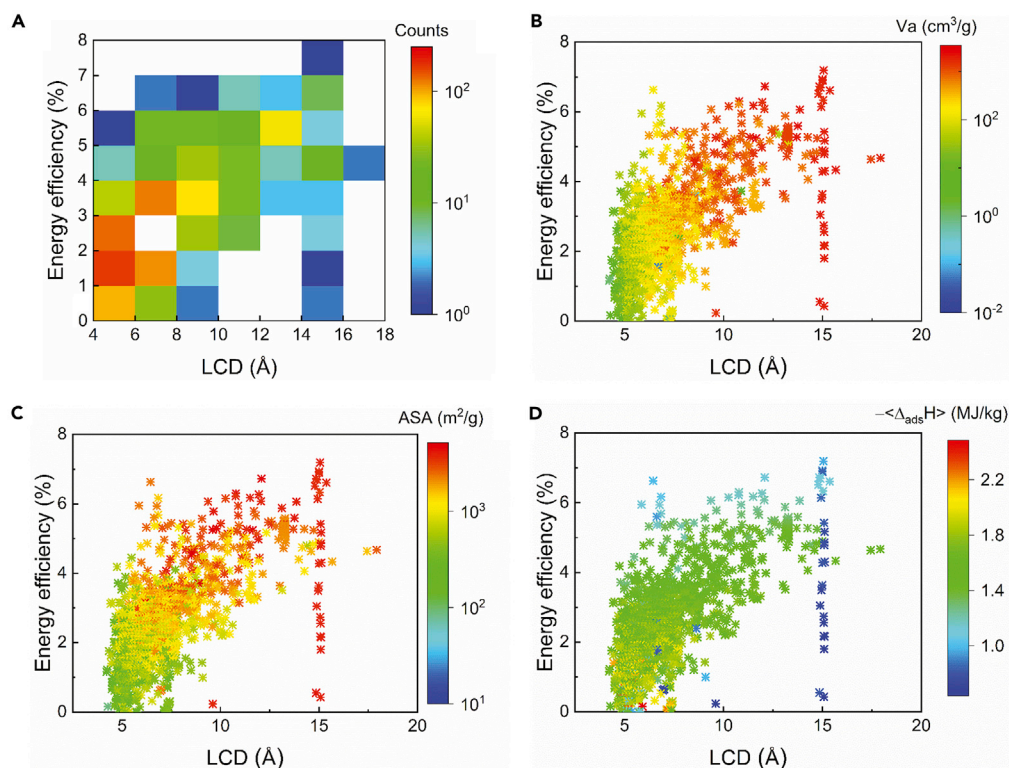
Figure 4. Predicted energy efficiency of 1322 CoRE MOFs as a function of LCD

The data were colored by (A) MOF numbers, (B) V_a, (C) ASA, and (D) $-\langle\Delta_{ads}H\rangle$. The number of the MOFs in each square was calculated with an interval of LCD = 2 Å and ΔW = 0.2 g/g.

According to Equation (4), at given working solution and concentration, the energy efficiency is mainly determined by the working capacity ΔW and enthalpy of adsorption $-\langle\Delta_{ads}H\rangle$. Therefore, we further investigated the relationship between energy efficiency, ΔW, and $\langle\Delta_{ads}H\rangle$ as shown in Figure 5, from which the energy efficiency exhibited a positive dependence on ΔW. Higher ΔW is favorable for the energy efficiency. When ΔW is greater than 0.2 g/g, the energy efficiency exceeds 5%, after which no obvious enhancement in energy efficiency with ΔW can be observed. Higher ΔW is beneficial for the work extracted since larger ΔW means the well separated salt solution which augments the extracted work in the power generation process. Furthermore, when $\langle\Delta_{ads}H\rangle$ is located between −0.8 and −1.4 MJ/kg, the energy efficiency is higher than 5%, implicating the moderate $\langle\Delta_{ads}H\rangle$ is preferential for energy efficiency. To further illustrate the impacts of structure property and adsorption performance of MOFs on the energy efficiency, principle component analysis (PCA) was conducted using four descriptors (LCD, ASA, ΔW, and $-\langle\Delta_{ads}H\rangle$) as shown in Figure 6. The obvious correlation between four descriptors and energy efficiency suggested that the large LCD and ASA, high ΔW, and moderate $\langle\Delta_{ads}H\rangle$ are favorable for energy efficiency. The increased energy efficiency with the LCD, ASA, and ΔW can be obviously observed in Figure 6A, which is consistent with previous phenomena that both large LCD and ASA are favorable for ΔW that in turn enhances the energy efficiency of adsorption-driven OHEs. In contrast, the energy efficiency is not increased with $-\langle\Delta_{ads}H\rangle$. Similar to the observation in Figure 5, either too high or too low $-\langle\Delta_{ads}H\rangle$ is not favorable for the energy efficiency owing to the low ΔW of MOFs with too high or too low $-\langle\Delta_{ads}H\rangle$ as shown in Figure 3D. On the contrary, the MOFs with moderate $-\langle\Delta_{ads}H\rangle$ are preferential for high ΔW, thus resulting in high energy efficiency of adsorption-driven OHEs as shown in Figure 6.

Henry's constant (K_H) that describes the affinity of adsorbents toward methanol at extremely low pressure is also considered. As shown in Figure 7, the energy efficiency first increases with K_H. At about $K_H = 10^{-5}$ mol/(kg·Pa), the maximum energy efficiency is achieved. Thereafter, the energy efficiency decreases with K_H. It is highly possible that MOFs with small K_H values are favorable for stepwise adsorption, which will benefit the working capacity of MOFs (Figure 7B) and thus improve the energy efficiency. Therefore, to guarantee a high energy efficiency, small K_H values and high working capacity are required. The selected
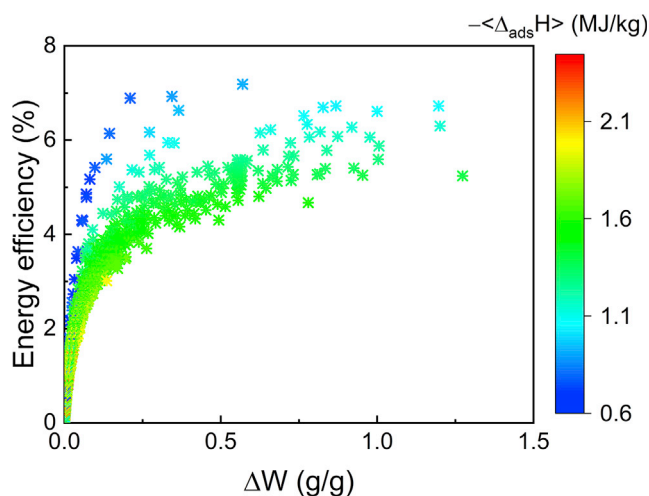
Figure 5. Predicted energy efficiency of 1322 CoRE MOFs as a function of δw colored by $-\langle\Delta_{ads}H\rangle$

top 10 MOFs exhibiting the highest energy efficiency were presented in Table S1, all of which possess small K_H, high LCD and ASA, and moderate $-\langle\Delta_{ads}H\rangle$ as demonstrated above. Experimental details on the synthesis, characterization, and methanol adsorption isotherm of the top performing MOFs were provided in Supplemental Information, indicating the consistency between GCMC simulation and experimental measurement.

Machine learning

Computational screening of high-performing MOFs from a vast number of MOF structures for the adsorption-driven OHE by GCMC simulations could still be time consuming. Machine learning offers an efficient approach to accelerate the screening processes via obtained data for training. The main structure properties of the MOFs determining the system performance are illustrated by LCD, ASA, Va, void fraction (VF), density, and K_H. Here, different machine learning models were employed to predict the energy efficiency by using the data of the 1322 CoRE MOFs obtained from high-throughput computational screening based on GCMC simulations. Eighty percent of the 1322 CoRE MOF data are randomly chosen for training and the remaining 20% are used for validation. The hyper-parameters of the machine learning models are adjusted by the Bayesian optimization with the acquisition function of expected-improvement-per-second-plus. Each machine learning model was trained 50 times to alleviate the random error, thus to accurately represent the quantitative correlation between descriptors and energy efficiency.
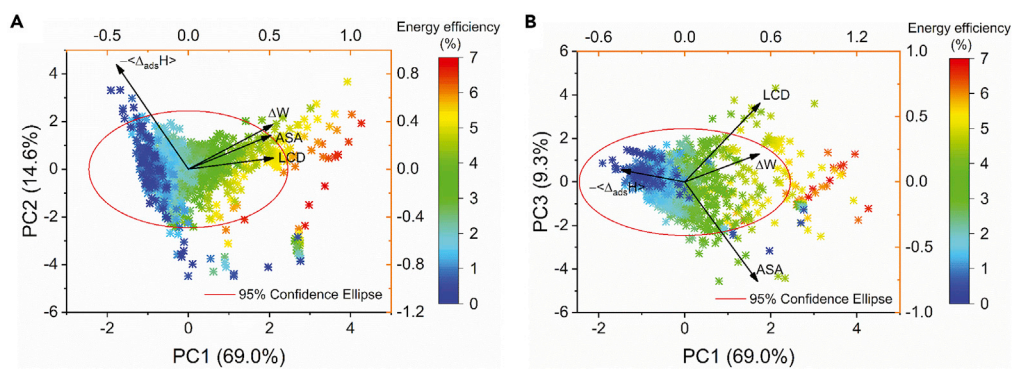
Figure 6. Principle component analysis (PCA) of the impacts of LCD, ASA, ΔW, and $\langle\Delta_{ads}H\rangle$ on the energy efficiency of 1322 CoRE MOFs
(A and B) (A) Based on the first and the second principle components and (B) based on the first and the third principle components.
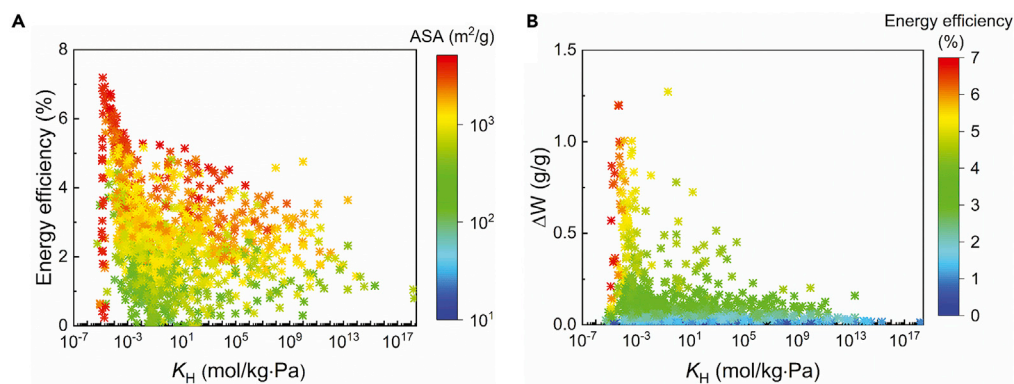
Figure 7. Relationship between energy efficiency and structure properties
(A and B) (A) Energy efficiency vs K_H colored by ASA; (B) working capacity vs K_H colored by energy efficiency.

As shown in Figure 8, classification machine learning models are employed to screen the desired MOFs via ensembles (boosted trees, bagged trees), k-nearest neighbor (KNN), decision trees (DTs), and support vector machines (SVMs). The hyper-parameters of the models are adjusted by the Bayesian optimization. Here, an energy efficiency above 5% is classified as high energy efficiency. An energy efficiency between 3% and 5% is defined as medium energy efficiency. The energy efficiency less than 3% is classified as low energy efficiency. The ensemble-based model shows the highest overall prediction accuracy of 88.3%, followed by the KNN, DT, and SVM models. By using the ensemble-based model, 91.7% of MOFs with the anticipated high energy efficiency (>5%) and 91.7% of the MOFs with undesired low energy efficiency (<3%) can be accurately predicted. The accuracy for predicting the MOFs with moderate energy efficiency is 78.9%. Although the overall prediction accuracy of the SVM model is the least for predicting the MOFs with moderate energy efficiency, 95.8% of MOFs with the anticipated high energy efficiency and 97.0% of the MOFs with undesired low energy efficiency can be predicted by the SVM model.

To step further, we conduct the regression machine learning to illustrate the quantitative relation of the structure properties of the MOFs with the energy efficiency via DTs, ensembles (boosted trees, bagged trees), Gaussian process, and SVM. R^2 was adopted to describe the accuracy of each model. As shown in Figure 9, despite the limited number of MOFs, the R^2 of all the chosen regression models is above 0.75. The highest accuracy of $R^2 = 0.84$ is obtained by the ensemble-based regression model, followed by the Gaussian process model ($R^2 = 0.79$) and DT model ($R^2 = 0.78$) and SVM model ($R^2 = 0.76$). Comparing to the predicted results by GCMC, 98 out of 120 MOFs with anticipated high energy efficiency (larger than 5%) are successfully identified in the ensemble-driven regression model. The deviation of predicted energy efficiency by the ensemble regression model from GCMC simulation is less than 1% for 98.6% of 1322 structures.

Compared to the computation time by GCMC, screening via machine learning exhibits overwhelming advantage. The time consumption for identifying one MOF structure via GCMC is several orders of magnitude larger than that via the machine learning, indicating the MOF screening could be dramatically accelerated via machine learning. Compared to the regression models, the classification models could offer more accurate predictions for high energy efficiency (>5%). In the SVM-based classification model, 95.8% of the anticipated high energy efficiency (>5%) obtained in the GCMC can be identified. In the ensemble-based regression model, 81.7% of the high energy efficiency (>5%) is identified.

However, the classification models can only predict the energy efficiency intervals via the MOF structure and properties and fail to predict the specific value of the energy efficiency. Therefore, the regression model was also used to identify the optimal structure properties of MOFs for energy efficiency. The GA is employed to conduct the optimization through the ensemble-based regression model with maximum energy efficiency as the objective function. Details of the optimization process can be found in the Supplemental Information. Optimal structure properties of the MOFs are LCD = 15.00 Å, VF = 0.84, ASA = 3583 m^2/g, V_a = 1682.88 cm^3/g, density = 0.6 g/cm^3, and $K_H = 3.75 \times 10^{-5}$ mol/kg/Pa. All the optimal structure properties are located in the suggested intervals in the aforementioned analysis. Due to the fitting errors of the machine learning, the maximum energy efficiency (6.53%) is slightly less than the maximum energy
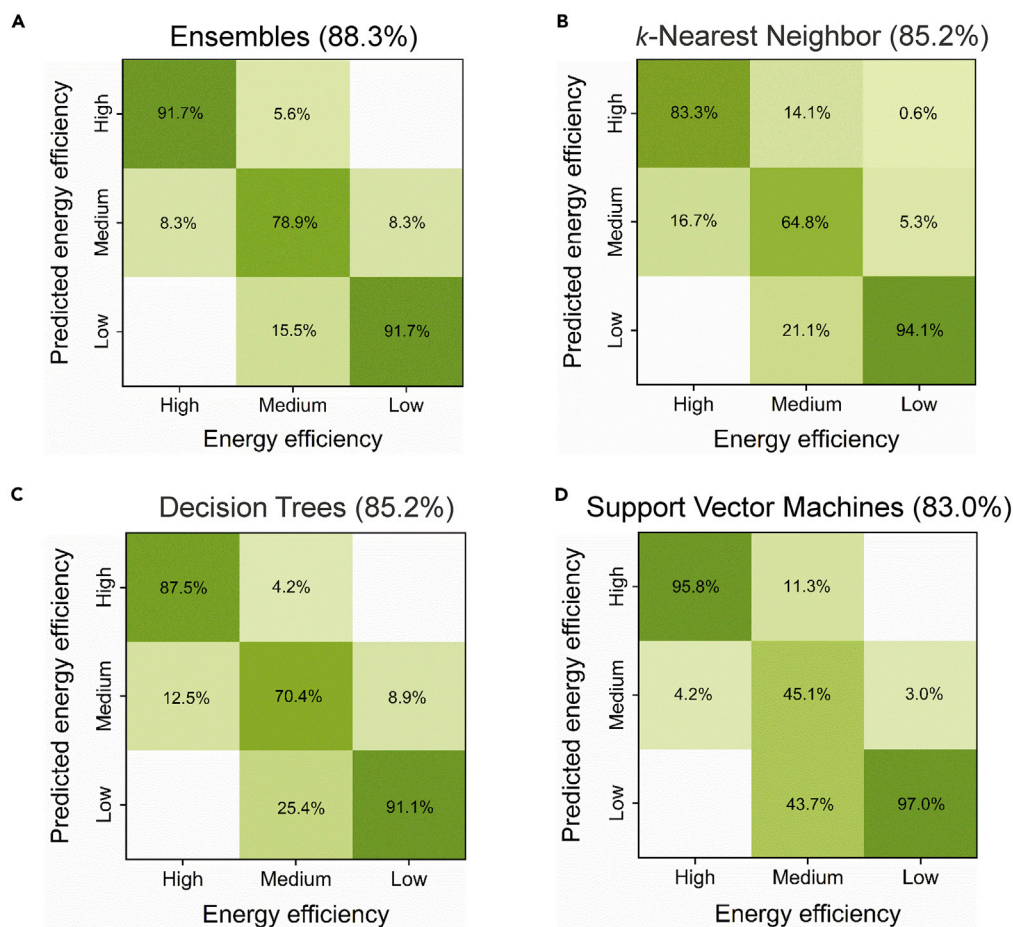
Figure 8. Confusion matrix for predictions of energy efficiency
(A–D) (A) Ensembles, (B) k-nearest neighbor (KNN), (C) decision trees (DTs), and (D) support vector machines (SVMs).

efficiency predicted using the GCMC simulations. The obtained optimal structure properties of MOFs could facilitate the rational design of efficient MOFs for upgraded heat-to-electricity conversion.

Conclusion

In this study, for the first time, a high-throughput computational screening based on GCMC was conducted to reveal the relationship between structure property of 1322 CoRE MOFs and the heat-to-electricity energy conversion efficiency for adsorption-driven OHEs under given operation conditions with LiCl-methanol as the working fluids. MOFs with LCDs between 8 Å and 16 Å exhibited the high working capacity and relatively low adsorption enthalpy, which are favorable for the energy efficiency. PCA analysis revealed that MOFs with the high working capacity, high pore size and surface area, and moderate adsorption enthalpy comparable to the evaporation enthalpy exhibited the high energy efficiency. Moreover, small K_H also benefits the energy efficiency possibly due to the presence of stepwise adsorption for MOFs with small K_H. Machine learning is also conducted to accelerate the computational screening of MOFs for adsorption-driven OHEs. The relationship between the energy efficiency and structure properties of MOFs (LCD, ASA, Va, VF, density, and K_H) is corelated via classification and regression machine learning models optimized by the Bayesian optimization. Compared to the regression models, the classification models could offer more accurate predictions for MOFs with high energy efficiency. The optimal structure properties of MOFs are identified via the ensemble-based regression model through the GA. It should be noted that the optimal structure properties are obtained based on the limited 1322 CoRE MOFs, which may vary as more MOFs are considered. Moreover, although the screening process was conducted under specific working conditions, the tendencies in the structure property relationship may be also applicable to
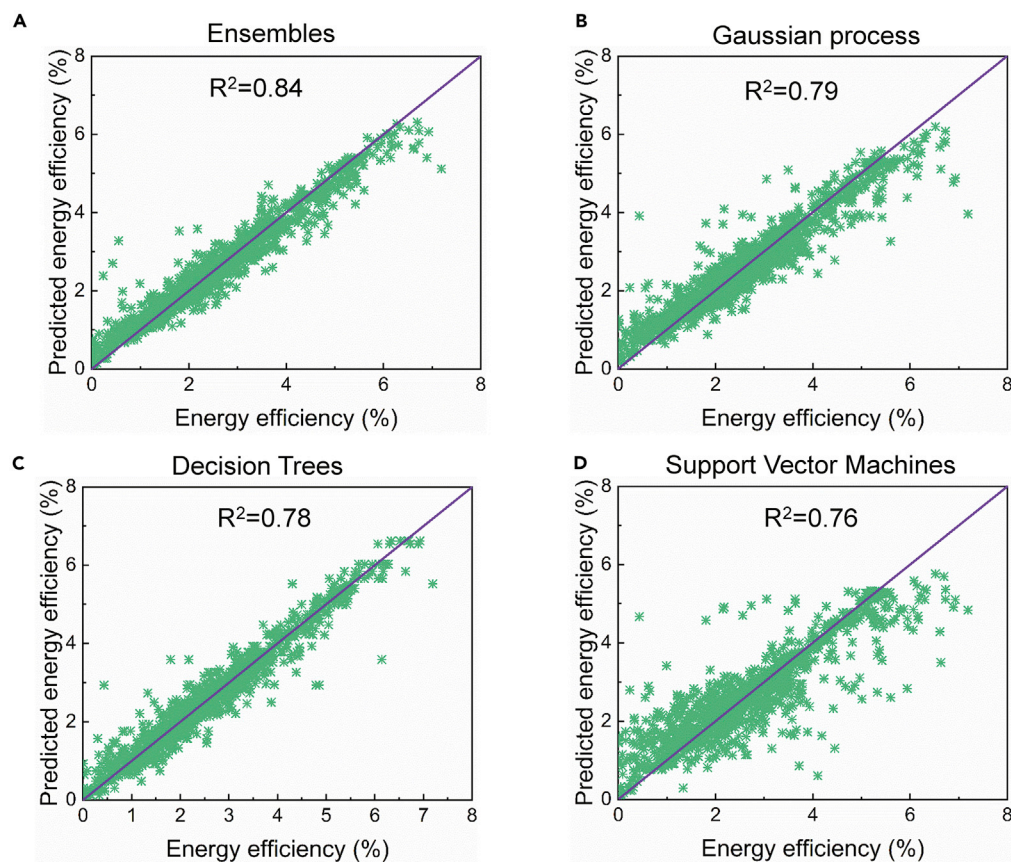
Figure 9. Energy efficiency predicated via various regression machine learning models
(A–D) (A) Ensembles, (B) Gaussian process, (C) decision trees, and (D) support vector machines.

different operating conditions and working concentrations of the LiCl-methanol solution. The structure-property relationship extracted from this work provides insightful guidance for quick exploration of high-performance MOFs and facilitates rational design of efficient MOFs for upgraded heat-to-electricity conversion of adsorption-driven OHEs.

Limitations of the study

This study screens MOFs for adsorption-driven OHEs via GCMC simulations and machine learning, which facilitates rational design and selection of efficient MOFs for upgraded heat-to-electricity conversion. In present study, the LiCl-methanol is employed as the working fluid. Future work is required to screen appropriate salt-methanol working fluids, thus to enhance the energy efficiency of the adsorption-driven OHEs. Futhermore, experimental studies can also be conducted to validate the obtained optimal MOF structure properties.

Resource availability

Lead contact

Further information and requests for resources and reagents should be directed to and will be fulfilled by the Lead Contact, Zhichun Liu (zcliu@hust.edu.cn)

Materials availability

This study did not generate new unique reagents.

Data and code availability

The data that support the findings of this study are available from the corresponding author upon reasonable request.

Methods

All methods can be found in the accompanying Transparent methods supplemental file.

Supplemental information

Supplemental information can be found online at https://doi.org/10.1016/j.isci.2020.101914.

Authors contribution

Conceptualization, R.L., Z.L., and S.L.; Writing – Original Draft, R.L.; Investigation, X.X.; Visualization, Y.Z.; Writing – Review & Editing, R.L. and S.L.; Supervision, Z.L. and W.L.

Declaration of interests

The authors declare no competing interests.

References

Altintas, C., Erucar, I., and Keskin, S. (2018). High-throughput computational screening of the metal organic framework database for CH4/H2 separations. ACS Appl. Mater. Interfaces 10, 3668–3679.

Bell, L.E. (2008). Cooling, heating, generating power, and recovering waste heat with thermoelectric systems. Science 321, 1457–1461.

Benjamin, J., Arias, M.E., and Zhang, Q.J.D. (2020). A techno-economic process model for pressure retarded osmosis based energy recovery in desalination plants. Desalination 476, 114218.

Canivet, J., Fateeva, A., Guo, Y., Coasne, B., and Farrusseng, D. (2014). Water adsorption in MOFs: fundamentals and applications. Chem. Soc. Rev. 43, 5594–5617.

Chanda, S., and Tsai, P.A. (2019). Numerical simulation of renewable power generation using reverse electrodialysis. Energy 176, 531–543.

Chen, G., Dresselhaus, M., Dresselhaus, G., Fleurial, J.-P., and Caillat, T. (2003). Recent developments in thermoelectric materials. Int. Mater. Rev. 48, 45–66.

Chu, S., and Majumdar, A. (2012). Opportunities and challenges for a sustainable energy future. Nature 488, 294–303.

Chua, H.T., Ng, K.C., Malek, A., Kashiwagi, T., Akisawa, A., and Saha, B.B. (1999). Modeling the performance of two-bed, silica gel-water adsorption chillers. Int. J. Refrigeration 22, 194–204.

Coasne, B., Galarneau, A., Pellenq, R.J.M., and Di Renzo, F. (2013). Adsorption, intrusion and freezing in porous silica: the view from the nanoscale. Chem. Soc. Rev. 42, 4141–4171.

Dakkama, H.J., Youssef, P.G., Al-Dadah, R.K., and Mahmoud, S. (2017). Adsorption ice making and water desalination system using metal organic frameworks/water pair. Energy Convers. Management 142, 53–61.

de Lange, M.F., Van Velzen, B.L., Ottevanger, C.P., Verouden, K.J.F.M., Lin, L.-C., Vlugt, T.J.H., Gascon, J., and Kapteijn, F. (2015a). Metal–organic frameworks in adsorption-driven heat pumps: the potential of alcohols as working fluids. Langmuir 31, 12783–12796.

de Lange, M.F., Verouden, K.J.F.M., Vlugt, T.J.H., Gascon, J., and Kapteijn, F. (2015b). Adsorption-driven heat pumps: the potential of metal–organic frameworks. Chem. Rev. 115, 12205–12250.

Erdős, M., De Lange, M.F., Kapteijn, F., Moultos, O.A., and Vlugt, T.J.H. (2018). In silico screening of metal–organic frameworks for adsorption-driven heat pumps and chillers. ACS Appl. Mater. Inter. 10, 27074–27087.

Forman, C., Muritala, I.K., Pardemann, R., and Meyer, B. (2016). Estimating the global waste heat potential. Renew. Sustainable Energy Rev. 57, 1568–1579.

Hu, J., Xu, S., Wu, X., Wu, D., Jin, D., Wang, P., Xu, L., and Leng, Q. (2019). Exergy analysis for the multi-effect distillation - reverse electrodialysis heat engine. Desalination 467, 158–169.

Kirchon, A., Day, G.S., Fang, Y., Banerjee, S., Ozdemir, O.K., and Zhou, H.-C. (2018). Suspension processing of microporous metal-organic frameworks: a scalable route to high-quality adsorbents. iScience 5, 30–37.

Lee, J.-G., Kim, Y.-D., Shim, S.-M., Im, B.-G., and Kim, W.-S. (2015). Numerical study of a hybrid multi-stage vacuum membrane distillation and pressure-retarded osmosis system. Desalination 363, 82–91.

Lee, S.W., Yang, Y., Lee, H.-W., Ghasemi, H., Kraemer, D., Chen, G., and Cui, Y. (2014). An electrochemical system for efficiently harvesting low-grade heat energy. Nat. Commun. 5, 3942.

Li, B., Li, S., Wang, B., Meng, Z., Wang, Y., Meng, Q., and Li, C. (2020a). Capture of sulfur mustard by pillar[5]arene: from host-guest complexation to efficient adsorption using nonporous adaptive crystals. iScience 23, 101443.

Li, Q., Omar, A., Cha-Umpong, W., Liu, Q., Li, X., Wen, J., Wang, Y., Razmjou, A., Guan, J., and Taylor, R.A. (2020b). The potential of hollow fiber vacuum multi-effect membrane distillation for brine treatment. Appl. Energy 276, 115437.

Li, S., Chung, Y.G., and Snurr, R.Q. (2016). High-throughput screening of metal–organic frameworks for CO2 capture in the presence of water. Langmuir 32, 10368–10376.

Li, W., Xia, X., Cao, M., and Li, S. (2019a). Structure–property relationship of metal–organic frameworks for alcohol-based adsorption-driven heat pumps via high-throughput computational screening. J. Mater. Chem. A 7, 7470–7479.

Li, Z., Xing, X., Meng, D., Wang, Z., Xue, J., Wang, R., Chu, J., Li, M., and Yang, Y. (2019b). Hierarchical structure with highly ordered macroporous-mesoporous metal-organic frameworks as dual function for CO2 fixation. iScience 15, 514–523.

Liu, X., Wang, X., and Kapteijn, F. (2020). Water and metal–organic frameworks: from interaction toward utilization. Chem. Rev. *120*, 8303–8377.

Long, R., Kuang, Z., Liu, Z., and Liu, W. (2019). Ionic thermal up-diffusion in nanofluidic salinity-gradient energy harvesting. Natl. Sci. Rev. *6*, 1266–1273.

Long, R., Lai, X., Liu, Z., and Liu, W. (2018). Direct contact membrane distillation system for waste heat recovery: modelling and multi-objective optimization. Energy *148*, 1060–1068.

Long, R., Li, B., Liu, Z., and Liu, W. (2017). Hybrid membrane distillation-reverse electrodialysis electricity generation system to harvest low-grade thermal energy. J. Membr. Sci. *525*, 107–115.

Long, R., Zhao, Y., Luo, Z., Li, L., Liu, Z., and Liu, W. (2020). Alternative thermal regenerative osmotic heat engines for low-grade heat harvesting. Energy *195*, 117042.

Olkis, C., Brandani, S., and Santori, G. (2019). A small-scale adsorption desalinator. Energy Proced. *158*, 1425–1430.

Olkis, C., Santori, G., and Brandani, S. (2018). An Adsorption Reverse Electrodialysis system for the

generation of electricity from low-grade heat. Appl. Energy *231*, 222–234.

Ortega-Delgado, B., Giacalone, F., Catrini, P., Cipollina, A., Piacentino, A., Tamburini, A., and Micale, G. (2019). Reverse electrodialysis heat engine with multi-effect distillation: exergy analysis and perspectives. Energy Convers. Management *194*, 140–159.

Post, J.W., Veerman, J., Hamelers, H.V.M., Euverink, G.J.W., Metz, S.J., Nymeijer, K., and Buisman, C.J.N. (2007). Salinity-gradient power: evaluation of pressure-retarded osmosis and reverse electrodialysis. J. Membr. Sci. *288*, 218–230.

Shi, Z., Liang, H., Yang, W., Liu, J., Liu, Z., and Qiao, Z. (2020). Machine learning and in silico discovery of metal-organic frameworks: methanol as a working fluid in adsorption-driven heat pumps and chillers. Chem. Eng. Sci. *214*, 115430.

Tamburini, A., Tedesco, M., Cipollina, A., Micale, G., Ciofalo, M., Papapetrou, M., Van Baak, W., and Piacentino, A. (2017). Reverse electrodialysis heat engine for sustainable power production. Appl. Energy *206*, 1334–1353.

Thu, K., Yanagi, H., Saha, B.B., and Ng, K.C. (2017). Performance investigation on a 4-bed

adsorption desalination cycle with internal heat recovery scheme. Desalination *402*, 88–96.

Tian, H., Wang, Y., Pei, Y., and Crittenden, J.C. (2020). Unique applications and improvements of reverse electrodialysis: a review and outlook. Appl. Energy *262*, 114482.

Tritt, T.M., and Subramanian, M. (2006). Thermoelectric materials, phenomena, and applications: a bird's eye view. MRS Bull. *31*, 188–198.

Wu, W., Shi, W., Wang, J., Wang, B., and Li, X. (2016). Experimental investigation on NH3–H2O compression-assisted absorption heat pump (CAHP) for low temperature heating under lower driving sources. Appl. Energy *176*, 258–271.

Zhao, Y., Li, M., Long, R., Liu, Z., and Liu, W. (2020a). Dynamic modelling and analysis of an adsorption-based power and cooling cogeneration system. Energy Convers. Management *222*, 113229.

Zhao, Y., Luo, Z., Long, R., Liu, Z., and Liu, W. (2020b). Performance evaluations of an adsorption-based power and cooling cogeneration system under different operative conditions and working fluids. Energy *204*, 117993.

Supplemental Information

Screening metal-organic frameworks for adsorption-driven

osmotic heat engines via grand canonical

Monte Carlo simulations and machine learning

Rui Long, Xiaoxiao Xia, Yanan Zhao, Song Li, Zhichun Liu, and Wei Liu

Supplemental Information

Table of Contents

This PDF file includes:

Supplementary Figures and Captions

Transparent Methods

Thermodynamic description of the adsorption-driven osmotic heat engine

Solution regeneration process. The isosteric diagram of the adsorption-driven regeneration cycle is presented in Figure 2, which consists of four steps, two for adsorption (isosteric cooling, isobaric adsorption) and two for desorption (isosteric heating, isobaric desorption). The temperatures during the evaporating and condensing processes are equal to the environmental temperature ($T_{eva}=T_{con}=T_{env}$). With salt dissolved in the solvent (Methanol in present study), the saturated pressure of the solvent decreases. Therefore, the evaporating pressure (P_{eva}) is lower than that of the condensing pressure (P_{con}).

Process 1-2: isosteric heating

The sorbent achieves it maximum adsorption capacity (W_{max}) of the solvent at point *I*. Before desorption, the sorbent should be heated to a certain temperature (T_2) so that the pressure is increased from P_{eva} to P_{con} for condensing. In this isosteric heating process, no solvent is released, and adsorbent vessel is disconnected from both the evaporator and condenser. Heat required is calculated as

$$Q_{1-2} = m_{sb}\int_{T_1}^{T_2} Cp^{eff}(T)dT + m_{sb}\int_{T_1}^{T_2} \rho_{liq}W_{max}Cp^{sol}(T)dT \tag{S1}$$

where Cp^{eff} is the effective specific heat of the sorbent with heat exchangers considered, which is assumed as the same as specific heat of the sorbent (1 kJ/(kg·K)) in present study. ρ_{liq} and Cp^{sol} are the density and specific heat capacity of adsorbed solvent, respectively.

Process 2-3: isobaric heating

When the pressure is increased to P_{con}, the sorbent is continuously heated meanwhile adsorbent vessel is connected to the condenser. The solvent is desorbed, and is then condensed in the condenser. The process stops when the temperature of the sorbent reaches the desorption temperature (T_{des}), where the working capacity of the adsorbent reaches its minimum value W_{min}. Heat needed in this isobaric process is given by

$$Q_{2-3} = m_{sb} \int_{T_2}^{T_3} Cp^{eff}(T)dT + m_{sb} \int_{T_2}^{T_3} \rho_{liq} \frac{W_{max} + W_{min}}{2} Cp^{sol}(T)dT - m_{sb}Q_{soprtion} \qquad (S2)$$

where $Q_{soprtion}$ is the extra energy needed during the desorption process.

$$Q_{soprtion} = \frac{1}{M_w} \int_{W_{min}}^{W_{max}} \rho_{liq}\Delta_{ads}H(W)dW \qquad (S3)$$

Process 3-4: isosteric cooling

Before beginning the adsorption process, the pressure should be decrease from P_{con} to P_{eva}, which is achieved by cooling the sorbent from T_3 to T_4. In this isosteric cooling process, no solvent is released, and adsorbent vessel is disconnected from both the evaporator and condenser. Heat released in this process is

$$Q_{3-4} = m_{sb} \int_{T_3}^{T_4} Cp^{eff}(T)dT + m_{sb} \int_{T_3}^{T_4} \rho_{liq}W_{min}Cp^{sol}(T)dT \qquad (S4)$$

Process 4-1: isobaric cooling

When the pressure is decreased to P_{con}, the sorbent is continuously cooled meanwhile adsorbent vessel is connected to the evaporator. The solvent is evaporated in the evaporator, and is then adsorbed by the sorbent. The process stops when the temperature of the sorbent decreases to T_1, where the working capacity of the sorbent reaches its maximum value W_{max}. Heat released in this isobaric process is given by

$$Q_{4-1} = m_{sb} \int_{T_4}^{T_1} Cp^{eff}(T)dT + m_{sb} \int_{T_4}^{T_1} \rho_{liq} \frac{W_{max} + W_{min}}{2} Cp^{sol}(T)dT - m_{sb}Q_{soprtion} \qquad (S5)$$

Total heat needed in the desorption process, named regeneration heat, is $Q_{reg} = Q_{1-2} + Q_{2-3}$. As the working capacity is much less than the mass of the sorbent, Q_{reg} can be simplified as

$$Q_{reg} \approx m_{sb}Cp^{sorbent}\Delta T - \frac{1}{M} m_{sb}\rho_{liq}\langle \Delta_{ads}H \rangle \Delta W \qquad (S6)$$

where the average adsorption enthalpy $\langle \Delta_{ads}H \rangle$ of the solvent can be calculated as

$$\langle \Delta_{ads}H \rangle = \frac{\Delta_{ads}H_{max} + \Delta_{ads}H_{min}}{2} \qquad (S7)$$

Maximu power extracted during the PRO process. In the PRO process, solvent from

the feed solution permeates through a semipermeable membrane into a pressurized draw solution at pressure P_{PRO}, and then is depressurized through a hydro turbine to generate electricity. The effluent concentration (C_f) of the draw solution is given by

$$C_f = \frac{C_0 V_0}{V_0 + \Delta V} \tag{S8}$$

where V_0, C_0 are respectively the inlet volume flow rate and concentration of the draw solution. ΔV is the transmembrane water flow rate. When the applied hydraulic pressure equals to the osmotic pressure ($P_{PRO} = \nu R \Phi T_H C_f$), water stops transferring through the membrane. Therefore, the power extracted in the PRO process is

$$P = P_{PRO} \Delta V = \nu R \Phi T \frac{C_0 V_0}{V_0 + \Delta V} \Delta V \tag{S9}$$

It increases with increasing ΔV. Under steady state operation, the maximum permeate flow should equal to that in the upstream adsorption-driven regeneration process. The final draw concentration is equal to the working concentration C_1. Then corresponding applied pressure in the PRO module is thus $P_{PRO} = \nu R \Phi T_H C_1$. The maximum power extractable is $P = \nu R \Phi T_1 C_1 \Delta V_{RO}$. Therefore, the maximum work can be calculated as

$$W_{extracted} = \frac{\nu R \Phi T_1 C_1 \Delta W m_{sb}}{\rho_{liq}} \tag{S10}$$

Energ efficiency of the adsorption-driven osmotic heat engine. Acording to aforementioned analysis, the heat needed is Q_{reg}, and the work extracted is

$W_{extracted} = \dfrac{\nu R \Phi T_1 C_1 \Delta W m_{sb}}{\rho_{liq}}$. Therefore, the energy efficiency is calculated as

$$\eta = \frac{W_{extracted}}{Q_{reg}} = \frac{\nu R \Phi T_1 C_1 \Delta W}{c_p^{sorbent} \Delta T - \dfrac{1}{M_w} \rho_{liq}^{wf} \langle \Delta_{ads} H \rangle \Delta W} \tag{S11}$$

Osmotic coefficient

The dimensionless osmotic coefficient Φ can be calculated using the following

equation (Pitzer and Mayorga, 1973)

$$\Phi - 1 = |Z_+ Z_-| f^\phi + m\left[(2v_+ v_-)/v\right]B^\phi + m^2\left[(2v_+ v_-)^{3/2}/v\right]C^\phi \tag{S12}$$

where Z is the ion charge, v is the number of ions. m is the molality. And the other coefficients are listed below

$$f^\phi = -A_\phi I^{1/2}/(1+bI^{1/2}) \tag{S13}$$

$$B^\phi = \beta^{(0)} + \beta^{(1)}\exp\left(-\alpha_1 I^{1/2}\right) + \beta^{(2)}\exp\left(-\alpha_2 I^{1/2}\right) \tag{S14}$$

$$A_\phi = (1/3)(2\pi N\rho)^{1/2}\left(e^2/4\pi\varepsilon_0\varepsilon kT\right)^{3/2} \tag{S15}$$

where $\beta^{(0)}$, $\beta^{(1)}$, $\beta^{(2)}$, and C^ϕ are Pitzer's ion-interaction parameters. A_ϕ is the Debye-Huckel constant. α_1, α_2, and b are adjustable parameters. I is the ionic strength. N is Avogadro's number. e is the elementary charge, ε_0 is the vaccum permittivity, and k is the Boltzmann constant. ε the relative dielectric constant.

$\beta^{(0)} = -0.11458$, $\beta^{(1)} = -3.95303$, $\beta^{(2)} = 3.421$, $C^\phi = 0.06478$ (Zafarani-Moattar and Nasirzade, 1998).

Physical properties of Methanol

The density, relative dielectric constant, and heat capacity of the liquid methanol are given as (Haghbakhsh and Raeissi, 2018, Bezman et al., 1997)

$$\rho = \exp\left(A + BT + CT^2\right) \tag{S16}$$

$$\varepsilon = a + bT + cT^2 \tag{S17}$$

$$c_p = \left(C_1 + C_2 T + C_3 T^2\right)M^{-1} \tag{S18}$$

where $A = 0.08584$, $B = -9.60\times10^{-4}\,K^{-1}$, $C = -4.30\times10^{-7}\,K^{-2}$, $a = 37.909$, $a = -2.2838\times10^{-3}\,K^{-1}$, $c = 6.659\times10^{-4}\,K^{-2}$, $C_1 = 1.06\times10^5\,J\,kmol^{-1}K^{-1}$, $C_2 = -3.62\times10^2\,J\,kmol^{-1}K^{-2}$, and $C_3 = 9.38\times10^{-1}J\,kmol^{-1}K^{-3}$ (Haghbakhsh and Raeissi, 2018) (Bezman et al., 1997).

MOF structure property calculations

The computationally ready experimental (CoRE) MOF database consisting of 2932 structures with DFT-derived density-derived electrical and chemical(DDEC) atomic charges are used for accurately describing the methanol adsorption behavior in present study (Nazarian et al., 2016). After excluding the structures without accessible surface area (ASA) and working capacity, 1322 structures from the CoRE-MOF database are eventually employed for computational screening. The helium void fraction (VF) and Henry's constant (K_H) are obtained via the Widom insertion method in RASPA (Widom, 1963, Dubbeldam et al., 2016). The largest cavity diameter (LCD), ASA, and available pore volume (V_a) were calculated by using a nitrogen probe with a radius of 1.86 Å in Zeo++ 0.3 (Willems et al., 2012).

GCMC simulations

The GCMC simulations were performed for 1322 MOFs to compute the methanol adsorption uptake and heat of adsorption under specific operating conditions. The parameters for Lennard-Jones interactions of all the MOFs are from the universal force field (UFF) (Rappe et al., 1992) and the atomic charges are from DDEC charges(Manz and Sholl, 2010). The parameters of methanol were obtained from the transferable potentials for phase equilibria (TraPPE) force field (Chen et al., 2001). The reliability of illustrating the adsorption properties via the UFF and TraPPE force fields can be found in previous literatures (Nalaparaju et al., 2010, Bueno-Perez et al., 2017). For all the studied MOFs, more than 2×10^5 Monte Carlo cycles were performed for each

structure until the complete equilibration of methanol adsorption. In each cycle four Monte Carlo moves including insertion, deletion, rotation, and translation were implemented with equal probability. The methanol uptake and heat of adsorption were obtained from 1×10^5 cycles for production after equilibration.

Experimental details

Chemicals: All chemicals were used without any further purification after purchasing from commercial sources. Zinc nitrate hexahydrate ($Zn(NO_3)_2\cdot6H_2O$, 99 %), terephthalic acid (H_2BDC, 99 %) from Shanghai Aladdin Bio-Chem Technology Co., Ltd. N,N-dimethylformamide (DMF, AR), dichloromethane (CH_2Cl_2, AR) and anhydrous methanol from Sinopharm Chemical Reagent Co., Ltd. Nitrogen gases (N_2, 99.999 %) and helium gases (He, 99.999 %) from Huaerwen Industrial Co., Ltd.

Synthesis of EDUSIF (i.e. MOF-5). 2.25 g (7.50 mmol) of $Zn(NO_3)_2\cdot6H_2O$ and 0.415 g (2.50 mmol) of H_2BDC were dissolved in 245 mL of DMF and 5 mL deionized water in a 500 mL teflon-lined autoclave. The mixture was heated at 373 K for 7 h. After cooling to room temperature, the solvent was decanted. The remaining solid was washed with 250 mL of DMF six times in which the solid was soaked in DMF for 8 h each time. Then, the solid was washed six times with 250 mL of CH_2Cl_2 similarly to DMF. Finally, CH_2Cl_2 was decanted and the solid was dried under vacuum at 393 K for 12 h.

Characterization. Powder X-ray diffraction (PXRD) data were collected on an Empyrean X-ray diffractometer from PANalytical B.V. in reflection mode using Cu Kα (λ= 1.540598 Å) radiation at 1600 W (40 kV, 40 mA). The 2θ rangs from 5° to 50° as a continuous scan with a step size of 0.01313° at room temperature. N_2 adsorption isotherm was measured at 77 K on an Autosorb-iQ2 from Quantachrome Instruments. MOF-5 was activated at 393 K for 24 h under vacuum before measurement. Brunauer-Emmett-Teller (BET) surface area was determined by fitting the BET model to the collected N_2 adsorption isotherm. Total pore volume was calculated by the N_2 uptake

at $P/P_0 = 0.993$, where P_0 is the saturation pressure of N_2 at 77 K.

Methanol adsorption isotherm measurement. Adsorption isotherm of methanol vapor was measured at 293 K on an Autosorb-iQ2 gas analyzer from Quantachrome Instruments. Anhydrous methanol was added into the vapor generator as the vapor source. MOF-5 was activated at 393 K for 24 h to remove water and other impurities before the measurement. Adsorption isotherm was collected from 0.01 to 12 kPa.

Machine learning details

The Details of the classification and regression machine learning models used in present study are listed in Table S3 and Table S4. Indicators (R^2, RMSE, and MAE) of regression machine learning models are included in Table S5. The learning curve for the ensemble-based regression model is depicted in Figure S5.

Optimization process based the genetic algorithm

The genetic algorithm (GA) originates from the theory of the natural selection in the biological genetic progress. It can be applied to complex optimization problems. The optimizable parameters are encoded as chromosomes, which forms a population. The GA employs selection, crossover and mutation to randomly generate populations, which are terminated while the stopping criterion is fulfilled, meanwhile the optimal solutions are obtained. As shown in Figure S6, firstly, we calculate energy efficiency of each MOF via GCMC and thermodynamic analysis. Then, regression machine learning models are employed to achieve the relation between the structure and adsorption properties of the MOFs and the energy efficiency. Base on the obtained regression, GA is used to obtain the optimal structure and adsorption properties with maximum energy efficiency as the objective function.

Table S1. Top 10 MOFs selected with efficiency ≥ 6.3%. Related to Figure 5.

MOF code	LCD (Å)	VF (-)	ASA (m^2/g)	Va (cm^3/g)	Density (g/cm^3)	K_H (mol/kg/Pa)	ΔW (g/g)	$<\Delta_{ads}H>$ (MJ/kg)	Energy efficiency
EDUSIF	15.05	0.83	3674.7	1721.3	0.59	1.41E-05	0.57	-0.96	7.19%
VUSKEA	15.00	0.83	3611.3	1709.2	0.59	1.98E-05	0.34	-0.94	6.93%
MIBQAR18	15.00	0.84	3639.1	1726.0	0.60	1.30E-05	0.21	-0.83	6.89%
PEVQEO	14.84	0.84	3573.9	1685.6	0.61	1.51E-05	0.87	-1.08	6.73%
XEBHOC	12.08	0.86	4637.1	2172.9	0.47	5.25E-05	1.20	-1.10	6.73%
PEVQIS	14.89	0.81	3571.6	1632.9	0.61	2.44E-05	0.83	-1.08	6.70%
RONZID	6.45	0.63	2315.4	143.0	1.11	2.68E-05	0.37	-1.00	6.63%
HAFTOZ	15.37	0.81	3571.8	1810.3	0.55	5.82E-05	1.00	-1.11	6.61%
PEVQOY	14.79	0.83	3527.6	1642.3	0.61	1.83E-05	0.77	-1.11	6.52%
IRMOF-6	15.03	0.80	3143.0	1442.9	0.65	2.32E-05	0.78	-1.14	6.34%

Table S2. Structure properties from experiment measurement and simulations.

Related to Figure 5.

EDUSIF	BET surface area (m^2/g)	Total pore volume (cm^3/g)
Experiment	1948	0.9428
Simulation	3661	1.2155

Table S3. Details of the classification machine learning models. Related to Figure 8.

Models	Optimizable Hyper-parameters	Optimized Hyper-parameters
Ensembles	1. Ensemble method 2. Maximum number of splits 3. Number of learners 4. Learning rate 5. Number of predictors to sample	Ensemble method: Bag Leaners: 62 Maximum number of splits :408 Number of predictors to sample: 3
KNN	1. Number of neighbors 2. Distance metric 3. Distance weight 4. Standardize	Number of neighbors: 46 Distance metric: City block Distance weight: Squared inverse Standardize: Ture
SVM	1. Kernel function 2. Box constraint level 3. Kernel scale 4. Multiclass method 5. Standardize data	Multiclass method: One-vs-One Box constraint 0.0177 Kernel function: Polynomial Polynomial order: 3 Standardize data: true
Decision Trees	1. Maximum number of splits 2. Split criterion	Maximum number of splits: 35 Split criterion: Ginis diversity index

Table S4. Details of the regression machine learning models. Related to Figure 9.

Models	Optimizable Hyper-parameters	Optimized Hyper-parameters
Ensembles	1. Ensemble method 2. Minimum leaf size 3. Number of learners 4. Learning rate 5. Number of predictors to sample	Ensemble method：Bag Leaners: 471 Minimum leaf size:1 Number of predictors to sample: 6
GPR	1. Basis function 2. Kernel function 3. Kernel scale 4. Sigma 5. Standardize	Basis function: Zero Kernel function: RationalQuadratic Sigma: 0.1367 Standardize: true
SVM	-	-
Decision Trees	Minimum leaf size	Minimum leaf size: 1

Note: The hyper-parameters of the SVM model are default ones in the Matlab software for poor performance under the Bayesian optimization of the hyper-parameters.

Table S5. Indicators of regression machine learning models. Related to Figure 9.

Model	RMSE	R^2	MAE
Ensemble	0.0057	0.84	0.0043
GS	0.0061	0.79	0.0047
SVM	0.0067	0.76	0.0048
DT	0.0067	0.78	0.0049
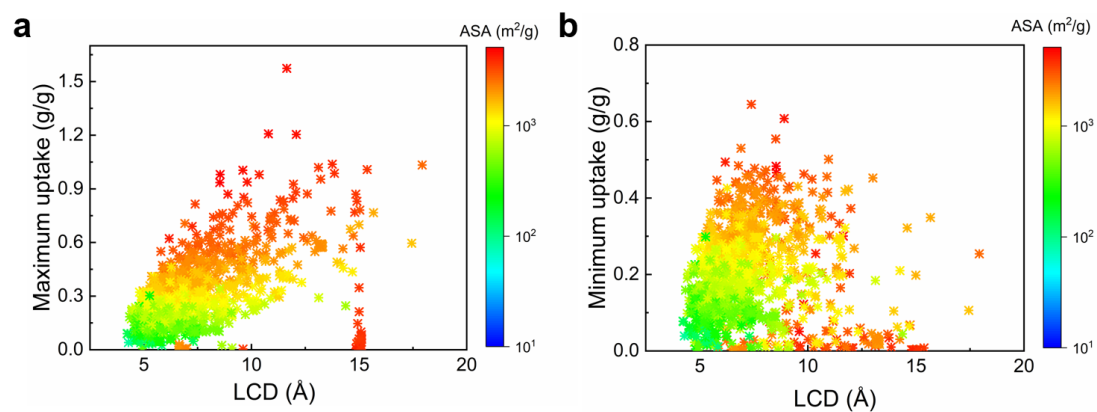
Figure S1. The predicted adsorption uptake of 1322 CoRE MOFs. (a) maximum and (b) minimum values of adsorption uptake as a function of LCD colored by ASA. Related to Figure 3.
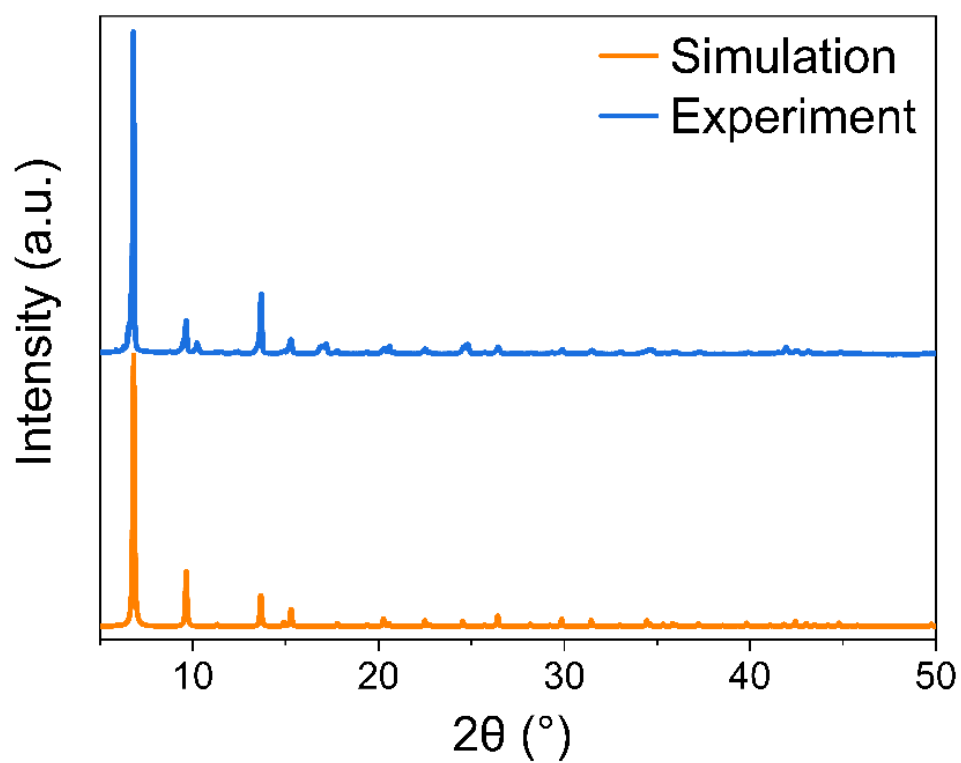
Figure S2. PXRD patterns of EDUSIF from simulation and experimental measurement. Related to Figure 5.
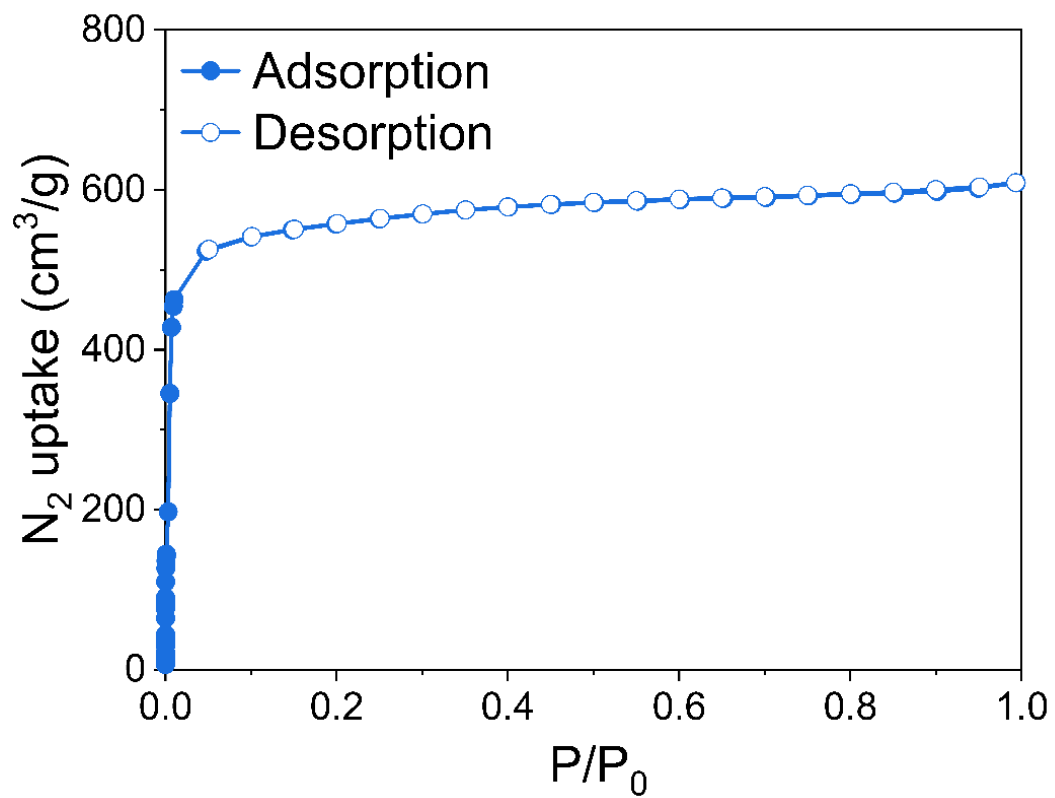
Figure S3. N_2 adsorption isotherms of EDUSIF at 77 K. Related to Figure 5.
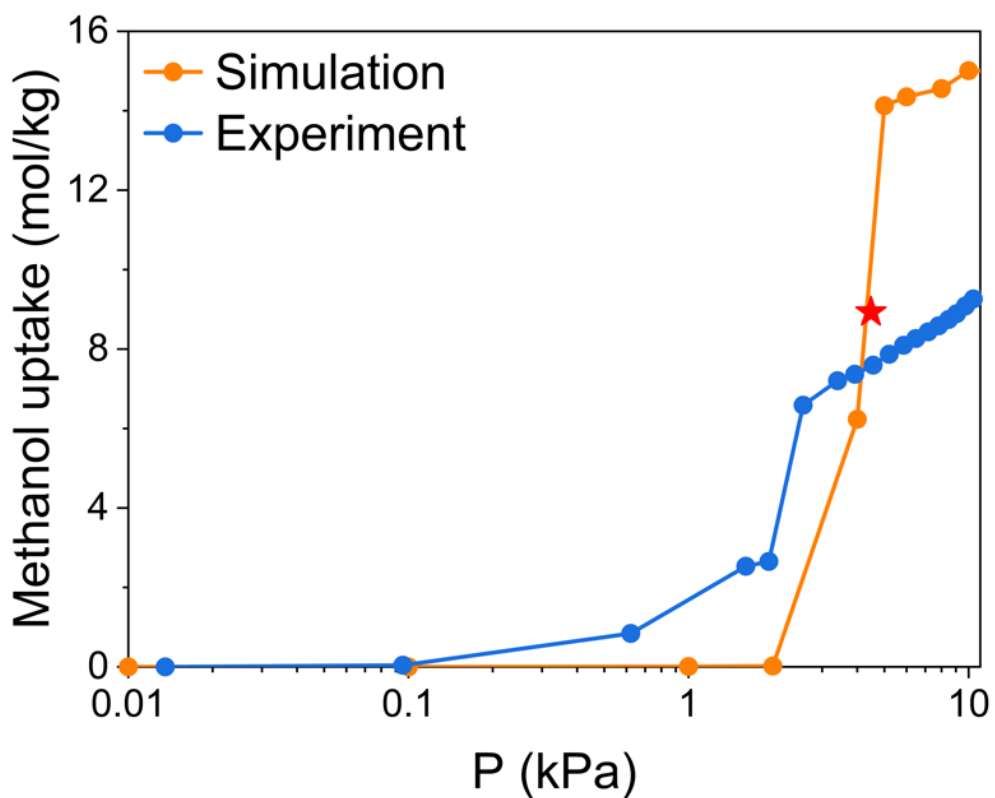
Figure S4. Adsorption isotherms of selected EDUSIF from GCMC simulations and experiment measurement at 293.15K. Related to Figure 5.

It should be noted that the simulated adsorption isotherm was scaled by 0.53 due to the reduced surface area of synthesized EDUSIF compared with perfect EDUSIF crystal used in simulations. The red star represents the simulated results at adsorption pressure (i.e. 4.480 kPa) after scaling.
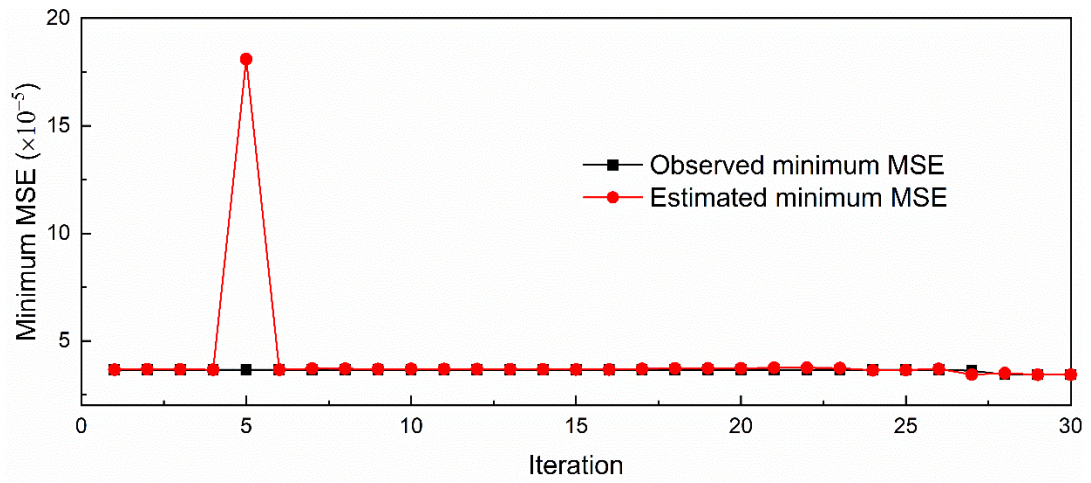
Figure S5. Learning curves of the ensemble-based regression model. Related to Figure 9.
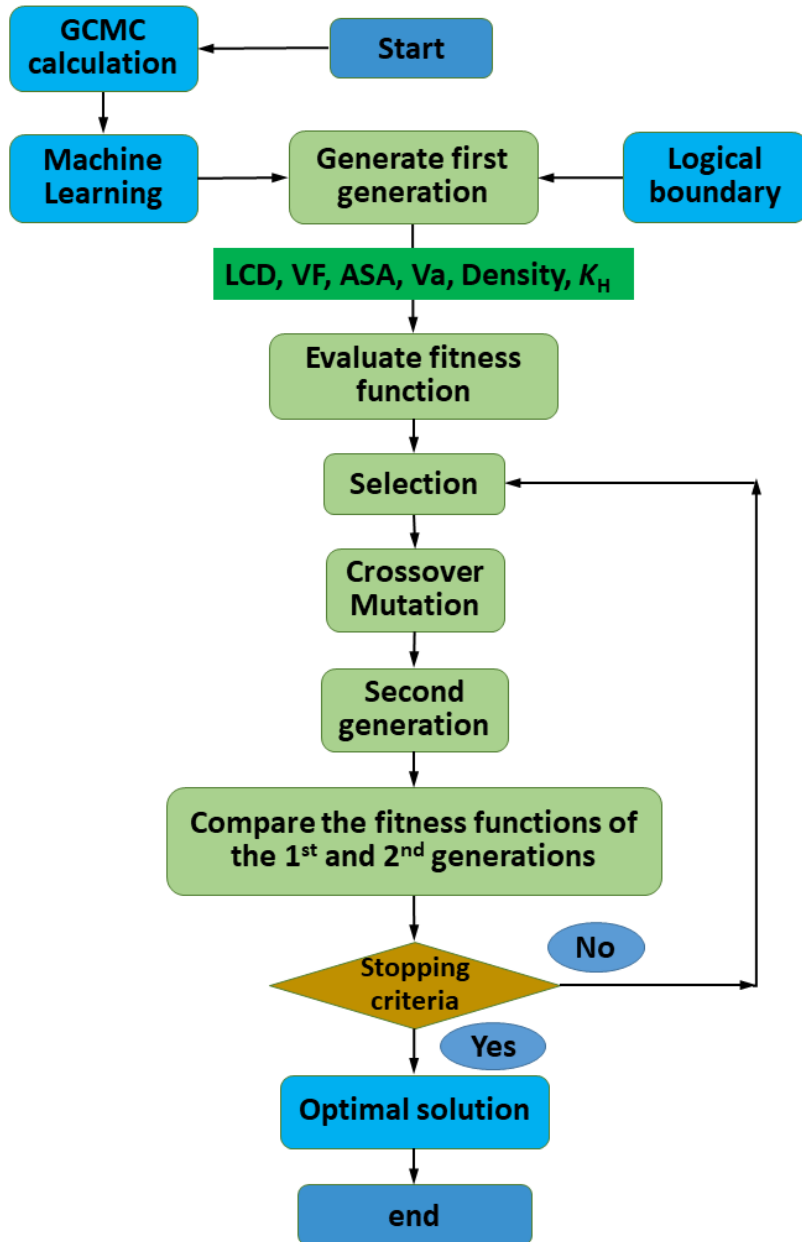
Figure S6. Flowchart of the GA optimization process. Related to Figure 9.

Supplemental references

BEZMAN, R. D., CASASSA, E. F. & KAY, R. L. 1997. The temperature dependence of the dielectric constants of alkanols. *Journal of Molecular Liquids,* 73-74**,** 397-402.

BUENO-PEREZ, R., MERKLING, P. J., GóMEZ-ÁLVAREZ, P. & CALERO, S. 2017. Cadmium–BINOL Metal–Organic Framework for the Separation of Alcohol Isomers. *Chemistry – A European Journal,* 23**,** 874-885.

CHEN, B., POTOFF, J. J. & SIEPMANN, J. I. 2001. Monte Carlo Calculations for Alcohols and Their Mixtures with Alkanes. Transferable Potentials for Phase Equilibria. 5. United-Atom Description of Primary, Secondary, and Tertiary Alcohols. *The Journal of Physical Chemistry B,* 105**,** 3093-3104.

DUBBELDAM, D., CALERO, S., ELLIS, D. E. & SNURR, R. Q. 2016. RASPA: molecular simulation software for adsorption and diffusion in flexible nanoporous materials. *Molecular Simulation,* 42**,** 81-101.

HAGHBAKHSH, R. & RAEISSI, S. 2018. Densities and volumetric properties of (choline chloride + urea) deep eutectic solvent and methanol mixtures in the temperature range of 293.15–323.15 K. *The Journal of Chemical Thermodynamics,* 124**,** 10-20.

MANZ, T. A. & SHOLL, D. S. 2010. Chemically meaningful atomic charges that reproduce the electrostatic potential in periodic and nonperiodic materials. *Journal of Chemical Theory and Computation,* 6**,** 2455-2468.

NALAPARAJU, A., ZHAO, X. S. & JIANG, J. W. 2010. Molecular Understanding for the Adsorption of Water and Alcohols in Hydrophilic and Hydrophobic Zeolitic Metal−Organic Frameworks. *The Journal of Physical Chemistry C,* 114**,** 11542-11550.

NAZARIAN, D., CAMP, J. S. & SHOLL, D. S. 2016. A Comprehensive Set of High-Quality Point Charges for Simulations of Metal–Organic Frameworks. *Chemistry of Materials,* 28**,** 785-793.

PITZER, K. S. & MAYORGA, G. 1973. Thermodynamics of electrolytes. II. Activity and osmotic coefficients for strong electrolytes with one or both ions univalent.

The Journal of Physical Chemistry, 77**,** 2300-2308.

RAPPE, A. K., CASEWIT, C. J., COLWELL, K. S., GODDARD, W. A. & SKIFF, W. M. 1992. UFF, a full periodic table force field for molecular mechanics and molecular dynamics simulations. *Journal of the American Chemical Society,* 114**,** 10024-10035.

WIDOM, B. 1963. Some Topics in the Theory of Fluids. *The Journal of Chemical Physics,* 39**,** 2808-2812.

WILLEMS, T. F., RYCROFT, C. H., KAZI, M., MEZA, J. C. & HARANCZYK, M. 2012. Algorithms and tools for high-throughput geometry-based analysis of crystalline porous materials. *Microporous and Mesoporous Materials,* 149**,** 134-141.

ZAFARANI-MOATTAR, M. T. & NASIRZADE, K. 1998. Osmotic Coefficient of Methanol + LiCl, + LiBr, and + LiCH3COO at 25 °C. *Journal of Chemical & Engineering Data,* 43**,** 215-219.